Analysis of transferred MoS_2 layers grown by MOCVD: evidence of Mo vacancy related defect formation

B. Schoenaers[1,‡], A. Leonhardt[2,3,‡,*], A. N. Mehta[1,3], A. Stesmans[1], D. Chiappe[3¶], I. Asselberghs[3], I. Radu[3], C. Huyghebaert[3], S. De Gendt[2,3], M. Houssa[1], V. V. Afanas'ev[1]

[1]*Department of Physics and Astronomy, University of Leuven, 3001 Leuven, Belgium*

[2]*Department of Chemistry, University of Leuven, 3001 Leuven, Belgium*

[3]*Imec, Kapeldreef 75, 3001 Leuven, Belgium*

A low-temperature multi-frequency electron spin resonance (ESR) study has been carried out on 1, 3.5, and 6 layer thick MoS_2 films, grown by metal organic vapor deposition (MOCVD) and subsequently transferred on SiO_2/Si. This reveals the observation of a previously unreported, nearly isotropic signal at $g \approx 1.9998$ with corresponding spin center (spin $S = ½$) densities ranging from ~ 6×10^8 cm^{-2} to ~ 5×10^{11} cm^{-2}. The ESR investigation is closely combined with an in-depth analysis by an assortment of other experimental techniques, including atomic force microscopy (AFM), Rutherford backscattering spectrometry (RBS), x-ray photoelectron spectroscopy (XPS), and transmission electron microscopy (TEM), to ultimately result in the assignment of the ESR signal to a defect of intrinsic nature, most likely a Mo vacancy (V_{Mo}) related defect located at MoS_2 grain edges or boundaries. The oxidation of the 2D material at grain edges and boundaries combined with the applied water-based transfer procedure is demonstrated to play a crucial role in the generation of the newly observed defect, thus advising caution with the currently applied process method. The presented analysis, which combines a variety of experimental techniques, contributes to the fine-tuning of the CVD growth and transfer process of high-quality few-layer MoS_2 intended for next-generation nanoelectronic devices.

* Corresponding author: alessandra.leonhardt@imec.be

‡ Authors contributed equally

¶ Currently at ASM Microchemistry, Pietari Kalmin katu 3, F 2, 00560 Helsinki

I. Introduction

Two-dimensional (2D) transition metal dichalcogenides (TMDs) exhibit several outstanding properties [1-9] like, e.g., an ultrathin nature, high mechanical strength and flexibility, and an advantageous band gap compared to graphene. A variety of promising TMD-based applications have therefore been proposed in electronics, [10-12] photonics, [13] and chemical and biological sensing. [14, 15] Molybdenum disulfide (MoS_2) emerged as a particularly interesting TMD [1] as it features a direct band gap of ~ 1.85 eV in covalently bonded S-Mo-S monolayer (ML) form, [3, 4] making the 2D material especially useful for optoelectronic and nanoelectronic applications. [2, 10-13, 16, 17] Furthermore, novel TMD based MOSFET structures entail reduced short channel effects and lower power consumption compared to traditional Si-based devices, paving the way for ultra-scaled beyond-Si transistors. [2, 10-12, 16, 17] Moreover, the interlayer van der Waals bonding nature of the 2D sheets potentially allows for the creation of novel heterostructures with enhanced functionality through stacking of multiple 2D materials that are characterized by different mechanical, electrical, and optical properties. [18-20]

As is the case with other semiconductor materials, the presence of structural defects like grain boundaries and point defects in the 2D crystal lattice can considerably degrade the performance of MoS_2-based devices, resulting in an electron mobility significantly lower than the theoretical limit of ~ 410 cm^2/Vs. [2, 21-25] Because of their potentially negative impact, a wide variety of intrinsic defects like vacancies, interstitials, and antisites have therefore been extensively studied both theoretically [26-33] and experimentally. [26, 30, 34] Yet, from the positive side, careful tailoring of crystal defects can also open a pathway to the modification of key properties, such as the photoluminescence intensity, [35] contact

resistance, [36] and doping, [27] relevant for both the study of fundamental physics and logic device applications.

Defects of intrinsic and extrinsic nature can be introduced both during the growth of the 2D material and during its processing, be it intentional or not. In particular, the synthesis of large area 2D materials of high epitaxial quality is often linked to growth processes that employ high temperatures and device template substrates such as sapphire, incompatible with direct device processing. [21, 37] The incorporation of 2D layers in logic devices is therefore performed through a transfer step, which on the one hand decouples the harsh growth conditions and use of non-standard substrates from the integration of the 2D layers, but on the other hand can also potentially lead to a significant modification of the 2D material. Hence, defect characterization and, more specifically, the evaluation of the impact of the material growth and processing on its formation is considered indispensable in device technology research. In this respect, electron spin resonance (ESR) arises as a particularly useful technique for the atomic assessment and quantification of defects in 2D (TMD) layers due to its exceptional sensitivity and atomic selectivity.

Aiming at a better understanding of point defects in transferred few-layer MoS_2, this work reports on the first successful observation by multi-frequency ESR of a previously unreported nearly isotropic signal at $g \approx 1.9998$ in metal-organic chemical vapor deposition (MOCVD) grown MoS_2 transferred onto SiO_2/Si substrates. [21] A comprehensive comparison of the measured signal with previous ESR observations on bulk geological and synthetic sulfurized and CVD-grown MoS_2 [25, 38-42] and first principles simulations [43] is combined with an extensive analysis by various experimental techniques, including atomic force microscopy (AFM), Rutherford backscattering spectrometry (RBS), x-ray photoelectron spectroscopy (XPS), and transmission electron microscopy (TEM), to ultimately assign the

newly observed signal to a defect of intrinsic nature, most likely a Mo vacancy (V_{Mo}) related defect located at MoS_2 grain edges or boundaries. The oxidation at the grain edges and boundaries of the 2D material combined with the applied water-based transfer procedure is demonstrated to play a crucial role in the generation of the newly observed defect. The presented comprehensive analysis unveils essential insights for the development of CVD growth and transfer procedures of high-quality MoS_2 layers intended for promising future nanoelectronic applications.

II. Experimental details

A. Samples

The MoS_2 studied is grown using MOCVD on a c-plane sapphire template wafer, as described by Chiappe et al. [21] The layers are grown using a $Mo(CO)_6$ solid precursor and a gas mixture of high-purity N_2, H_2, and H_2S. During growth at temperatures ranging from 700 °C to 900 °C, the total pressure is kept constant at 20 Torr. After growth, the MoS_2 layers are subjected to a post deposition anneal under a H_2S/N_2 gas flow at a total pressure of 100 Torr at 1000 °C.

Three samples of different MoS_2 thicknesses are studied in this work by a variety of experimental techniques. A first sample consists of one monolayer (ML) MoS_2 obtained by performing a temperature controlled lateral etching step after a first time-controlled regular growth procedure, intended to create a high quality 1 ML MoS_2 by selectively etching away the second (partially completed) layer through increasing the temperature to > 800°C, hereby also inducing beneficial recrystallization of the firstly formed layer. [21] The second and third samples are thicker, i.e., 3.5 and 6 MoS_2 MLs, and grown by the time controlled method without a temperature controlled lateral etching step. [21] In addition to these

three extensively studied MoS_2 specimens, a fourth bilayer MoS_2 sample is grown by the time controlled MOCVD method and investigated in the TEM analysis of this work.

After the layer-controlled MOCVD growth process, transferring of the 2D films is started by first spin coating polymethyl methacrylate (PMMA) on top as a protective layer and laminating a thermal removal tape as support layer. This procedure is followed by a water-assisted delamination from the sapphire growth substrate in a heated ultrasound water bath at 80 °C. Next, dry bonding of the 2D material to the target substrate (90 nm thermally grown SiO_2 on Si or ALD grown Al_2O_3 on Si) is performed on a heated surface at 80 °C. The supporting tape is subsequently removed at 155 °C and the PMMA dissolved in acetone overnight. The samples are then cleaned with isopropanol. Figure 1 shows a simplified schematic of the growth and transfer procedure.

In addition to the MoS_2 specimens, a MoO_3 sample is investigated by XPS to further understand the generation of the defects currently being investigated (vide infra). For this purpose, a 2-nm-thick layer of MoO_3 is deposited by thermal evaporation on top of a SiO_2/Si substrate.

For current analysis, both the transferred MoS_2 and the MoO_3 samples are subjected to low temperature annealing at 200 °C for 3 h in low vacuum (~ 10^{-4} Torr) with a ramping rate of 2 °C/min in a Nabertherm furnace.

B. Characterization methods

After the MoS_2 layer transfer, for ESR purposes, parts of the SiO_2/Si substrates are cut into slices of ~ 2×9 mm^2 main area with the 9 mm edge along the Si $[0\bar{1}1]$ direction and the c-axis along the main face normal **n**. The slices are stacked with the Si substrate $[0\bar{1}1]$ direction of each slice pointing in the same 'up' direction. The ESR measurements are performed over the temperature (T) range 1.6 - 27 K by means of conventional continuous

wave absorption derivative X- (~ 8.9 GHz), K- (~ 20.4 GHz), and Q-band (~ 34.3 GHz) spectrometers using periodic modulation, $B_m cos(\omega_m t)$, at $\omega_m/2\pi \approx 100$ kHz of the applied magnetic field **B**. Accurate determination of defect densities and *g* values is aided by making use of a systematically co-mounted Si:P marker sample [g(4.3 K) = 1.99869 ± 0.00002; S = ½] [44]. Defect densities are determined by double numerical integration of the detected $dP_{\mu r}/dB$ signals, where $P_{\mu r}$ is the reflected microwave power.

The structural quality of the MoS_2 layers is investigated by AFM in tapping mode, with topography and phase being taken simultaneously in ambient conditions. All AFM measurements are performed on as-grown MoS_2 on sapphire substrates. The TEM analysis is carried out with a Titan G2 60-300 operated at 120 kV in STEM mode with a convergence angle of 23 mrad. The TEM specimens are prepared by transferring two small pieces of the bilayer MOCVD-grown MoS_2 film onto two Quantifoil TEM grids using a water-assisted (80 °C) delamination process. The PMMA support layer of the two specimens is removed in acetone (50 °C) followed by a rinse in isopropyl alcohol (IPA; 50 °C).

The RBS measurements are performed with a 6SDH Pelletron accelerator (National Electrostatics Corporation, NEC), using He^+ ions and a beam energy of 1.523 MeV. The collected data is analyzed using the in-house developed software “SA - numeric integration”. XPS measurements are carried out in the angle resolved mode using a Theta300 system from Thermo Instruments, where 16 spectra are recorded at exit angles between 22° and 78° with respect to **n** and subsequently integrated. The XPS observations are performed using a monochromatized Al Kα X-ray source (1486.6 eV) and a spot size of 400 µm. Atomic concentrations are obtained from peak deconvolution invoking mixed Gaussian-Lorentzian peaks and standard sensitivity factors.

III. Results and discussion

A. Spectral appearance of the ESR signal

As an illustration of the overall ESR results, Fig. 2 shows a comparison of K-band spectra for the 1, 3.5, and 6 ML MoS_2 samples recorded at 4.3 K for **B**//**n**. A similar, so far undocumented, nearly isotropic signal characterized by $g \approx 1.9998$ and K-band peak-to-peak linewidth (ΔB_{pp}) in the range of 1.2 - 2.2 G is observed in the three studied samples of different MoS_2 thickness. Henceforth, the newly observed signal will be referred to as LM2.

A careful analysis of the linewidth dependence of the LM2 signal on the ESR observational frequency (ν) is presented in Fig. 3 for the 3.5 ML MoS_2 sample. The multifrequency (X-, K-, and Q-band) study reveals a dominant inhomogeneous broadening characterized by an almost linear frequency dependence of ΔB_{pp}. The latter points to a Voigt-like lineshape, a convolution of the Lorentzian and Gaussian shape, instead of the more general Lorentzian shape. Dealing with a Voigt profile, the linewidth of the ESR signal can be accurately described by the expression [45]

$$\Delta B_{pp} = \frac{1}{2}\Delta B_{pp}^{L} + \sqrt{\frac{1}{4}\left(\Delta B_{pp}^{L}\right)^2 + \left(\Delta B_{pp}^{G}\right)^2}, \qquad (1)$$

where ΔB_{pp}^{L} and ΔB_{pp}^{G} are the linewidths of the constituent Lorentzian and Gaussian shapes, respectively. The dashed curve in Fig. 3 represents an optimized fitting of Eq. (1), revealing a residual Lorentzian width ($\nu \rightarrow 0$) ΔB_{pp}^{L} = 1.3 ± 0.2 G and Gaussian part $\Delta B_{pp}^{G}/\nu$ = 0.06 ± 0.01 G/GHz. The distinct Gaussian line broadening can most likely be ascribed to a stress induced g spread, presumably at grain boundaries and/or edges. [46]

As to the magnetic behavior of the newly observed signal, Fig. 4 shows the observed inverse signal intensity versus T over the range 1.6 – 27 K for the 3.5 ML MoS_2 specimen. The signal intensity corresponds to the area under the absorption curve of the LM2 signal and is

proportional to the magnetic susceptibility χ of the spin system which can, in general, be described by the Curie-Weiss law written as $\chi \propto (T - T_c)^{-1}$. From least-square linear fitting of the data (dashed line in Fig. 4), we find for the current case a close to zero Curie-Weiss temperature $T_c \approx 0$ K, the latter indicating a distinct paramagnetic behavior which points to a system of dilutely distributed spins with faint or negligible mutual interaction.

Crucial to the current analysis, ESR also allows for reliable quantification of the number of centers corresponding to the observed signals, performed, as outlined before, by double numerical integration of the $dP_{\mu r}/dB$ signal. A distinctly varying density is obtained, i.e., $(6 \pm 1) \times 10^8$ cm^{-2}, $(4.5 \pm 0.3) \times 10^{11}$ cm^{-2}, and $(5.0 \pm 0.7) \times 10^9$ cm^{-2} for the 1, 3, and 6 ML MoS_2, respectively, with the densities given per cm^2 SiO_2/Si substrate area covered by one or more MoS_2 layers.

In comparison with the results for the other two sample types, the high LM2 defect density found in the 3.5 ML MoS_2 sample may come as inconsistent. Accordingly, ESR measurements have been repeated, albeit much later, on a newly prepared 3.5 ML MoS_2 sample layer transferred from a similarly MOCVD-grown MoS_2 film. The result, in terms of LM2 defect density (in the $10^8 - 10^9$ cm^{-3} range), is now found to be more in line with the 1 ML and 6 ML MoS_2 data, indicating that the unique first 3.5 ML specimen's significantly higher defect density can be attributed to an as of yet undetermined transfer and/or growth related cause. For clarity, figures 3 and 4 have been composed – for reasons of sensitivity – using data from the initial 3.5 ML MoS_2 sample, of which a representative K-band ESR signal observed at 4.3 K is shown in Fig. 2.

B. Tracing the origin of the LM2 signal

Having observed the previously unknown LM2 ESR signal, the crucial quest as to its atomic origin emerges. The AFM images shown in Fig. 5 may serve as an illustration for the structural quality of the MoS_2 layers and provide an initial indication for the possible atomic origin of LM2. Figure 5 (a) exposes the excellent monolayer coverage of the 1 ML MoS_2 attained thanks to the successful temperature controlled etching step. [21] The observed topographical features in Fig. 5 (a) are originating from the atomic steps of the sapphire substrate and no additional second layer nucleation islands can be discerned. On the other hand, the AFM images of the 3 and 6 ML MoS_2 shown in Fig. 5 (b) and (c) respectively, reveal several grain edges and boundaries, linked to triangular growth on top of the closed basal plane. [30, 47] Notably, the grain edges and boundaries in Fig. 5 (c) corresponding to the 6 ML sample, are characterized by narrow brightly colored lines indicative for the presence of MoO_3 which is expected to form at the highly reactive edges and boundaries. [48, 49]

In looking for the origin of the newly observed ESR signal, we first note that since the LM2 signal is absent in a SiO_2/(100)Si/SiO_2 control sample, and given the high purity level typically attained in synthesizing MoS_2 layers, it likely concerns an intrinsic defect in MoS_2. Next, the rather 'high' defect density, especially for the 3.5 ML MoS_2, excludes right away the defect to originate from the very edges of the MoS_2 layers at the borders of the substrate. In this respect, the grain boundaries and grain edges emerge as a primary suspect for the location of the defect.

Generally, reliable atomic identification by ESR heavily relies on the observation of signal hyperfine structure. However, in the absence of any such resolved structure in the LM2 signal, the search for its origin may initially be guided by a comparison with previous ESR studies on a variety of bulk geological and synthetic MoS_2 samples [25, 38-42] and computational assessment of intrinsic MoS_2 defects. [43] Yet, no LM2-like spectrum appears

to be reported so far. Perhaps most pertinently, in a recent ESR study on few-layer MoS_2 produced by sulfurization directly on the Mo target substrate, [25] the anisotropic (*g* value varying from 2.00145 to 2.0027) signal - denoted LM1 - has been observed, which was attributed to the S_{Mo} antisite defect (S substituting for Mo) located at grain boundaries. Although the LM1 and LM2 signals are distinctly different, on spectroscopic grounds, the LM2 signal can presumably still be attributed to a defect of intrinsic nature residing at grain boundaries or edges. Furthermore, a comparison of the measured *g* value with those obtained from first principle simulation of a set of intrinsic defects, [43] would allow for two possibilities as to the atomic defect nature of LM2: the observed LM2 *g* value ($g \approx 1.9998$) is reasonably close to both the one calculated for V_{Mo} ($g \approx 1.994$) and that for S_{Mo} ($g \approx 2.004$). Now, as the previously observed LM1 signal in sulfurized MoS_2 has been assigned to S_{Mo} and is spectroscopically well distinct from the current LM2 ESR signal, the latter is, purely from an ESR perspective, tentatively assigned to the V_{Mo} defect.

Pertinent to this interpretation though, it should be added that previous experimental work, using atomic resolution annular dark field (ADF) imaging, has found that V_{MoS3} is much more prevalent than V_{Mo} in CVD grown monolayer MoS_2. [30] Therefore, keeping in mind that the specific CVD growth conditions are known to be specifically determinative for the resulting material quality attained and the abundance of certain defects, the LM2 signal might be comprised of both the V_{Mo} and V_{MoS3} components. Yet, the STEM-ADF findings in recent work [30] only concern V_{Mo}/V_{MoS3} defects at an 'inner' layer position which is different from the presumed location of the currently observed defect, i. e., at grain boundaries or edges, urging great caution in the direct comparison of the present results with those of the previous STEM-ADF analysis. [30] While in the 'inner' region of the grains, sulfur vacancies and V_{MoS3} have been suggested to be dominant, grain boundaries and edges

can accommodate a large variety of defects and dislocations. Therefore, the ESR-observed defect in this work will henceforth be referred to as 'V_{Mo} related' since further theoretical and experimental investigation is required to determine the exact atomic structure of the point defect, most likely located at grain edges or boundaries and possibly distinct from an 'inner' layer V_{Mo} or V_{MoS3} defect.

The assignment of the LM2 signal to a V_{Mo} related defect is further substantiated by the RBS data shown in Fig. 6, demonstrating a noticeable increase of the S/Mo ratio after transfer of the MoS_2 material from the sapphire growth substrate to the SiO_2/Si target substrate. The increase of the S/Mo ratio is ascribed to a Mo loss since an increase in S atoms is unlikely in ambient conditions. As to the presumed mechanism of Mo loss, MoO_3 is expected to form primarily at grain boundaries and edges, [48, 49] as also shown in Fig. 5 (c), and most likely subsequently dissolved during the wet transfer process in hot (80 °C) water. [50, 51] Furthermore, the RBS data in Fig. 6 demonstrate that a 200 °C anneal in vacuum after transfer induces an additional loss of Mo. The latter RBS observation is firmly corroborated by XPS measurements shown in Fig. 7 on pure MoO_3 layers. The reduction in peak intensity and shift towards higher binding energy is consistent with a conversion of MoO_3 to MoO_x suboxides and concomitant loss of Mo after a 200 °C anneal in vacuum. This indicates that not only hot water but also low temperature (~ 200 °C) anneal in vacuum can induce chemical modifications in MOCVD-grown MoS_2 layers. One more observation pertinent to tracing the nature of the LM2 ESR signal, the current RBS analysis suggests that there must be at least some transfer induced V_{Mo} component to the LM2 signal as only an increasing number of V_{Mo} defects would lead to an increase of the observed S/Mo ratio.

So far, the oxidation – and subsequent dissolution – of grain edges and boundaries is concluded to play an important role in the generation of the V_{Mo} related defect. To get a

better understanding of the oxidation behavior of the MoS_2 material, and thus possibly aid the identification of the LM2 signal, an oxidative etching [48, 51] TEM analysis has been carried out on a bilayer MoS_2 sample grown by the time controlled MOCVD method. [21] Figure 8 shows a comparison of TEM images of the bilayer MoS_2 material demonstrating the influence of a short anneal of 5 min at 250 °C in air preceded by a rinse in warm water (50 °C) to oxidatively etch and change the morphology of the MoS_2 layers. The TEM images in panels (a) and (c) in Fig. 8 expose, as a result of the rinse and anneal procedure, the appearance of holes in the first MoS_2 monolayer which are seemingly located at grain boundaries and, interestingly, predominantly close to the edges of the second layer grains. Furthermore, panel (d) in Fig. 8 shows a representative degradation of the relatively sharp second layer grain edges (panel (b)) after the rinse and anneal procedure. The current TEM findings reveal an aggressive oxidative etching, particularly at the grain edges and boundaries, similar to what has been reported in a recent STEM study performed to reveal the kinetics for oxidative etching in monolayer CVD-grown MoS_2 by heating the 2D material in air. [48] This dramatic effect further substantiates our argument of process-induced defect generation at grain boundaries and edges. While a number of point defects can be generated by the growth (e.g. V_S, V_{MoS3}, etc), the processing significantly alters the MoS_2 morphology and generates further uncontrolled defects.

In addressing the atomic structure of the grain edges, Fig. 9 (a) shows a high resolution TEM image of a representative abundantly present second layer zigzag Mo edge (ZZ-Mo), [48, 52] with, in the current case, an additional S atom bonded to each edge-terminating Mo atom, as schematically demonstrated in Fig. 9 (b). The presence of the additional S edge atoms is attributed to the post deposition anneal in H_2S/N_2 performed after MOCVD growth. Additional S edge atoms aside, the nature of the most abundant edge structure, i.e., ZZ-Mo,

is similar to what has been reported in the previously mentioned recent oxidative etching study. [48] Crucially, this recent study advances, as an oxidation mechanism for the abundant ZZ-Mo edge, that the oxygen molecules initially bond with unsaturated Mo atoms, generating Mo vacancies leaving unsaturated S atoms. Since the ZZ-Mo edge is energetically more stable than the ZZ-S edge, the reaction continues along the S terminated directions to result in a terrace like ZZ-Mo edge structure. [48] To be noticed is that the proposed oxidative reaction pathway provides a plausible explanation for the current generation of the V_{Mo} related or, put differently, unsaturated S-bonds nature of the LM2 defect. The aggressive oxidative etching process can essentially be seen as a significantly accelerated version of the current situation where the MoS_2 edges oxidize and are subsequently subjected to a MoO_3 dissolving transfer procedure in hot water (80 °C). Moreover, a similar reaction pathway can be considered for the grain boundaries as it has been demonstrated before that the oxidative etching occurs in a similar way at this location. [48] Nevertheless, further complications arise in the unambiguous identification of the LM2 signal at grain boundaries as these are known to contain complex 4|4, 4|7, 5|7, and 6|8 dislocation core structures. [30] However, as these samples are grown on a sapphire template, the predominant grain boundary structure is dominated by 60° rotational twins which usually only consist of 4|4 and 4|8 structures, as shown in Fig. 9 (d).

Admittedly, the exact determination of the atomic structure of the newly revealed defect located at grain edges or boundaries proves to be an arduous task. The current extensive analysis, combining a variety of experimental techniques, does however provide reasonable evidence for the V_{Mo} related nature of the LM2 defect along with suggesting a plausible generation mechanism, thus establishing a basic platform for future theoretical and experimental endeavor.

C. Influence of the growth conditions on the V_{Mo} related defect formation

Thus far we have evaluated the appearance of the newly observed LM2 ESR signal in MOCVD-grown few-layer MoS_2 transferred on SiO_2/Si and attributed it to a V_{Mo} related defect at grain boundaries or edges. However, at first sight, no obvious correlation is observed between the V_{Mo} related defect densities and the respective number of MoS_2 layers. The remarkably different defect densities, varying by up to almost three orders of magnitude, over the different MoS_2 thicknesses studied can however be tentatively attributed to the specific layer-by-layer MOCVD growth method which requires a meticulous control of the growth temperature and, crucially, deposition time to allow for the growth of high quality uniform 2D layers. [21]

As discussed before, two MOCVD growth approaches have been implemented: The 3.5 and 6 ML MoS_2 are grown by the time-controlled method and the 1 ML MoS_2 is grown by including a temperature controlled lateral etching step in the regular MOCVD growth procedure. The latter approach allows for the selective removal of the (partially completed) defective top layer. [21] In the current work, the 1 ML MoS_2 is supposedly of the highest epitaxial quality, as also demonstrated by its AFM image (Fig. 5 (a)), with the lowest V_{Mo} related defect density at grain boundaries or edges due to the successful application of a lateral etching step. The defect density for the 6 ML MoS_2 sample is also relatively low, most likely due to a beneficial complicated recrystallization process during the MOCVD growth, resulting in a material of decent epitaxial quality. On the other hand, the 3.5 ML MoS_2 is tentatively demonstrated to be of the lowest epitaxial quality as it exhibits the highest V_{Mo} related defect density out of the three studied samples, which is attributed to the absence of a temperature controlled lateral etching step and possibly less extensive recrystallization of the underlying MoS_2 layers when compared to the 6ML MoS_2 specimen.

Regardless of the intricate growth mechanisms at play, the particular growth process can supposedly enhance the generation of V_{Mo} related defects either by providing a higher density of grain edges and boundaries at which the V_{Mo} related defect can form or by making the boundaries and edges more susceptible to oxidation and subsequent Mo loss during the wet transfer procedure. In fact, a combination of both effects also seems plausible. Yet, due to the MOCVD growth procedure inherently being delicate and complex, a detailed investigation of the influence of the specific growth conditions on the formation of the V_{Mo} related defect is set aside for future work.

IV. Conclusions

In summary, a low-*T* multi-frequency ESR study on MOCVD-grown few-layer MoS_2 transferred on a SiO_2/Si substrate revealed a previously unreported nearly isotropic signal characterized by g ≈ 1.9998 and ΔB_{pp} in the range of 1.2 - 2.2 G at K-band. Aided by AFM, RBS, XPS and TEM observations, the newly observed LM2 signal is attributed to a defect of intrinsic nature, more specifically a V_{Mo} related defect located at grain edges or boundaries. The wet transfer procedure is shown to play a crucial role in the generation of the V_{Mo} related defect as MoO_3 is expected to form primarily at grain edges and boundaries and then to be subsequently dissolved in hot (80 °C) water, thus causing a loss of Mo. An annealing procedure in vacuum at 200 °C is also demonstrated to induce a loss of Mo.

The LM2 defect densities of the 1, 3.5, and 6 ML MoS_2 vary by almost three orders of magnitude, ranging from ~ 6×10^8 cm^{-2} to ~ 5×10^{11} cm^{-2}. The 1 ML MoS_2 is shown to be of the highest epitaxial quality showing excellent 1 ML coverage and lowest ESR-inferred defect density which are both most likely related to the successful application of a lateral etching step in the MOCVD growth process. The 6 ML MoS_2 also appears to be of decent epitaxial

quality ascribed to a beneficial complicated recrystallization taking place during the MOCVD growth. The specific MOCVD growth procedure is demonstrated to alter the oxidation behavior of the 2D material, subsequent loss of Mo during the wet transfer, and concomitant generation of V_{Mo} related defects.

The current study provides essential insights for further development of MOCVD growth and transfer procedures to obtain a high-quality 2D MoS_2 material, partly in that it urges great caution with water-based transfers and highlights possible chemical instabilities of few-layer MoS_2 during thermal treatments.

Figure captions

Figure 1: Simplified schematic of layer growth and transfer procedures. MoS_2 layers are grown by MOCVD on sapphire templates, and then covered with a PMMA and thermal release tape (not shown). MoS_2 is delaminated from sapphire through hot water intercalation, and subsequently bonded to the target substrate at 80 °C. The thermal release tape is removed at 155 °C, and the PMMA dissolved in acetone and IPA at room temperature.

Figure 2: Derivative-absorption K-band ESR spectra $dP_{\mu r}/dB$ of MOCVD grown 1, 3, and 6 ML MoS_2 films transferred onto thermal SiO_2/Si showing the observation of a nearly isotropic signal at $g \approx 1.9998$ denoted by LM2. The newly observed signal is ascribed to a V_{Mo} related defect at grain edges or boundaries. The spectra are relatively scaled to their respective total covered substrate surface area after transfer. The signal at $g = 1.99869$ stems from a co-mounted Si:P marker sample.

Figure 3: Frequency dependence of the peak-to-peak linewidth ΔB_{pp} of the LM2 signal observed in 3.5 ML MoS_2 by ESR at 4.3 - 11 K for **B**//**n**. The linewidth analysis reveals a dominant inhomogeneous broadening characterized by an almost linear frequency dependence of the linewidth on the observational frequency. The dashed curve represents an optimized fitting of Eq. (1), revealing a residual Lorentzian width ($\nu \rightarrow 0$) $\Delta B_{pp}^{L} = 1.3 \pm 0.2$ G and Gaussian broadening $\Delta B_{pp}^{G}/\nu = 0.06 \pm 0.01$ G/GHz. Error bars denote the spread on the data of multiple observations.

Figure 4: Temperature dependence of the inverse K-band ESR intensity (double integral of $dP_{\mu r}/dB$) of the LM2 signal assigned to a V_{Mo} related defect in the 3.5 ML MoS_2 sample. The dashed line represents an optimized linear fitting of the Curie-Weiss law ($\chi \propto (T$

$- T_c)^{-1}$) demonstrating a nearly paramagnetic ($\chi \propto T^{-1}$) behavior with a close to zero $T_C \approx 0$ K. Error bars denote the spread on the data of multiple observations.

Figure 5: Comparative AFM analysis of the 1, 3.5, and 6 ML MoS_2 films on c-plane sapphire substrates. Panel (a) shows the AFM topography of the 1 ML MoS_2 sample grown by an MOCVD process including a temperature controlled lateral etching step. The etching-based procedure results in an excellent monolayer coverage of the sapphire substrate. The terraces that are visible in the topography originate from the sapphire substrate. The AFM topography of the 3.5 and 6 ML MoS_2 samples is shown in panel (b) and (c) respectively. Both MoS_2 specimens are grown by the time-controlled MOCVD process and exhibit islands forming one or more layers that are not closed.

Figure 6: Plot showing the S to Mo ratio (S/Mo) determined by RBS before and after transferring the MoS_2 layers to the target SiO_2/Si substrate. The S/Mo ratio increases after transfer with an additional increase after exposing the transferred layers to a 200 °C anneal in vacuum. The increase of the S to Mo ratio is ascribed to a loss of Mo. 'NA' stands for 'no anneal'. Error bars are calculated from the statistical uncertainties of the RBS measurements.

Figure 7: Overlay of XPS spectra of the Mo3d region of MoO_3 samples, highlighting the reduction in peak intensity and peak transition to higher binding energy after the sample is subjected to a 200 °C anneal in vacuum. The XPS spectra demonstrate the partial conversion of MoO_3 to molybdenum sub-oxides and concomitant loss of Mo due to the anneal in vacuum.

Figure 8: TEM image comparison of a MOCVD-grown bilayer MoS_2 specimen before (a, b) and after (c, d) a warm water rinse at 50 °C followed by an anneal in air at 250 °C. The

dark spots in panel (c) represent holes formed in the first monolayer that are mainly located at grain boundaries and close to the second layer grain edges. A representative degradation of the relatively sharp edges of a second layer grain is demonstrated in panel (d).

Figure 9: Panel (a) shows an atomic resolution TEM image of a representative abundantly present second layer ZZ-Mo edge with an additional S atom bonded to each terminating Mo edge atom. The atomic model in panel (b) serves as an illustration for the current ZZ-Mo edge structure. The TEM intensity profile along the white dashed line in panel (a) is presented in panel (c). Panel (d) shows the predominant grain boundary structure which is dominated by 60° rotational twins which usually only consist of 4|4 and 4|8 structures.

Figures

Figure 1

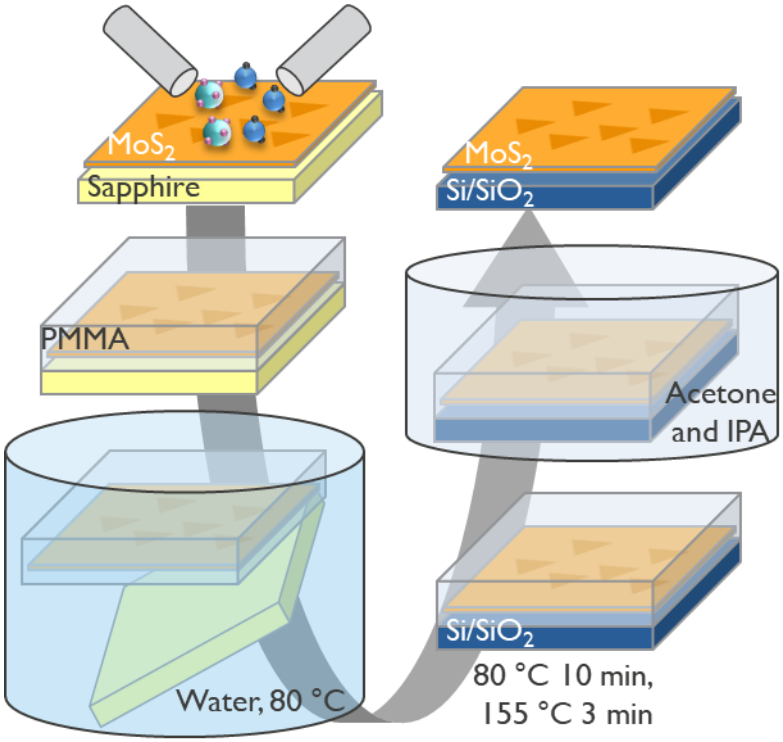

Figure 2

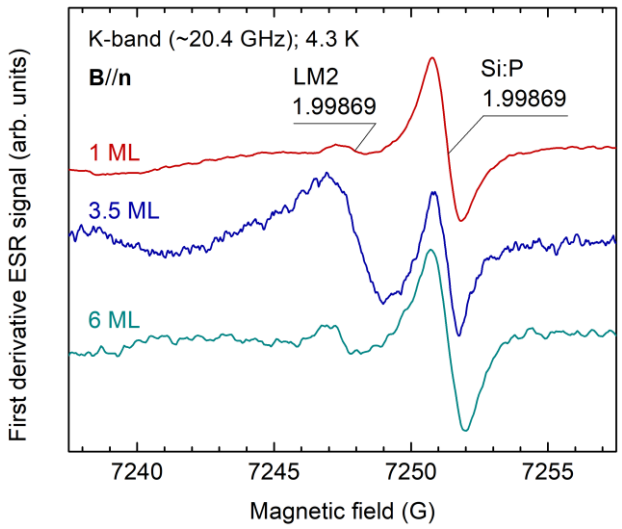

Figure 3

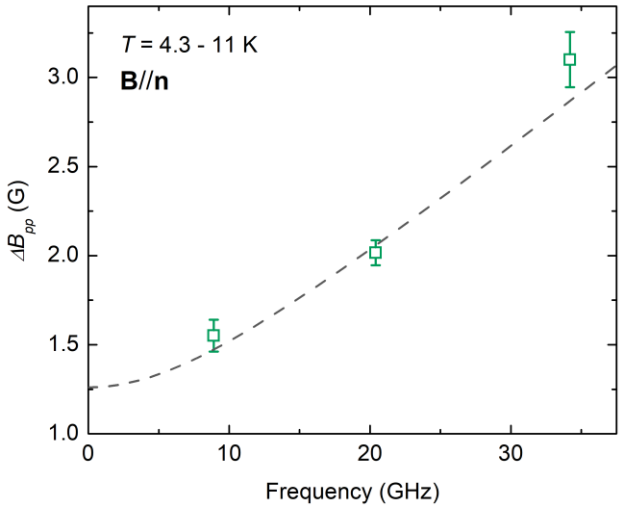

Figure 4

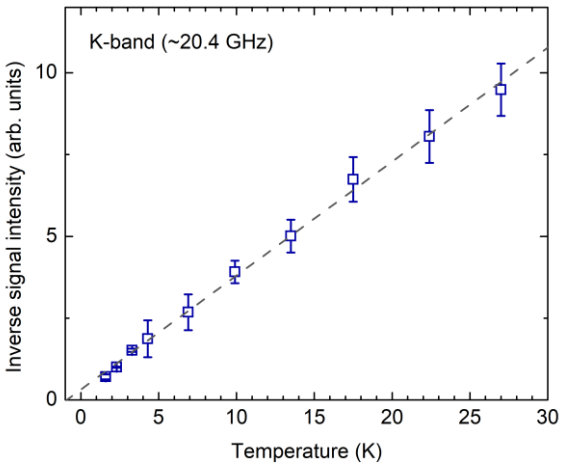

Figure 5

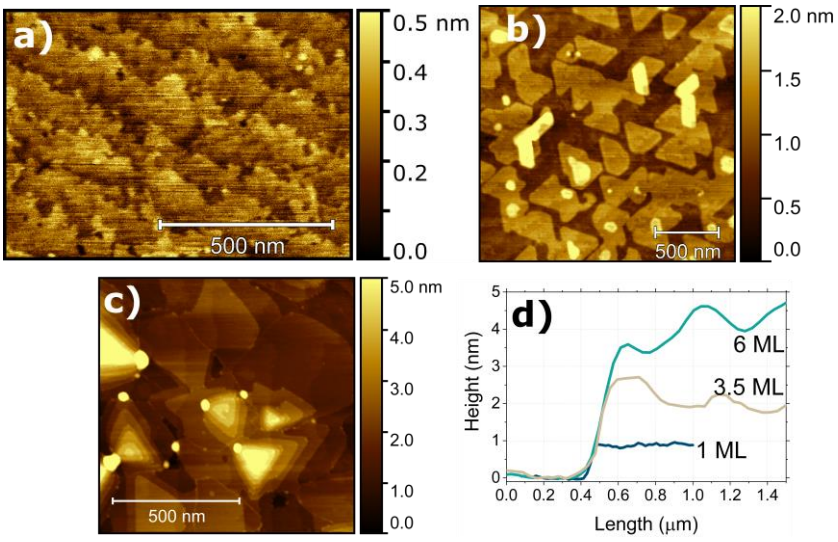

Figure 6

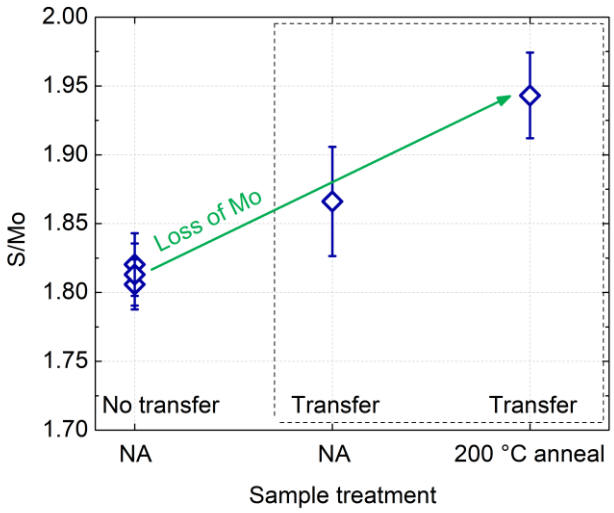

Figure 7

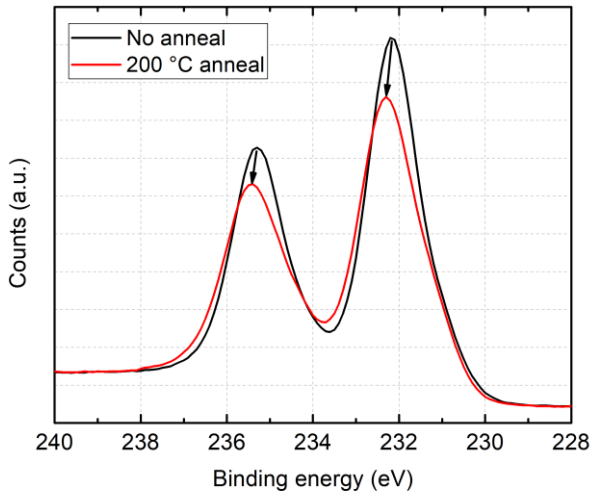

Figure 8

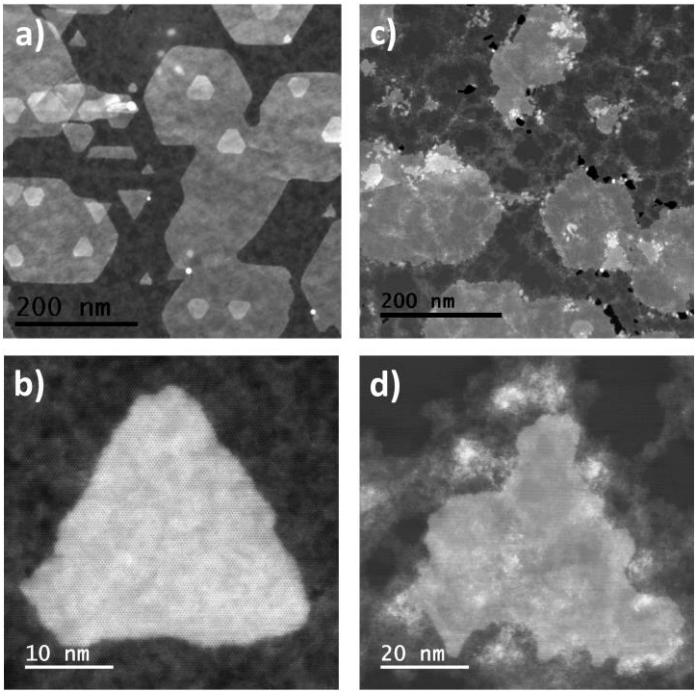

Figure 9

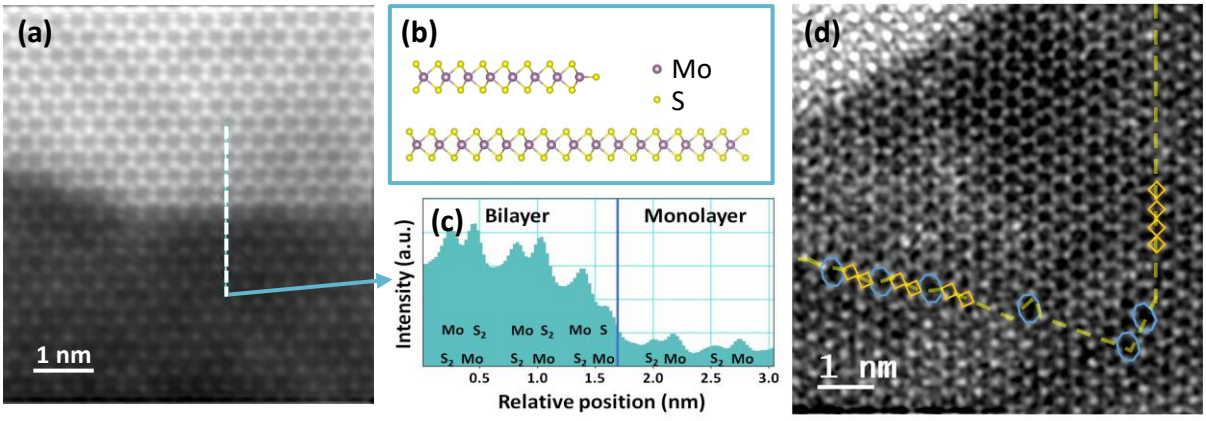

References

[1] S. Manzeli, D. Ovchinnikov, D. Pasquier, O. V. Yazyev, and A. Kis, Nat. Rev. Mater. 2, 17033 (2017).

[2] B. Radisavljevic, A. Radenovic, J. Brivio, V. Giacometti, and A. Kis, Nat. Nanotechnol. 6, 147 (2011).

[3] Q. H. Wang, K. Kalantar-Zadeh, A. Kis, J. N. Coleman, and M. S. Strano, Nat. Nanotechnol. 7, 699 (2012).

[4] D. Voiry, A. Mohite, and M. Chhowalla, Chem. Soc. Rev. 44, 2702 (2015).

[5] I. Song, C. Parkab, and H. C. Choi, RSC Adv. 5, 7495 (2015).

[6] S. McDonnell, R. Addou, C. L. Hinkle, and R. M. Wallace, in *2D Materials for Nanoelectronics*, edited by M. Houssa, A. Dimoulas, and A. Molle (Taylor and Francis, LLC, Boca Raton, 2016), p. 163.

[7] A. H. Castro Neto and K. Novoselov, Mater. Express 1, 10 (2011).

[8] J.-G. Song, G. H. Ryu, S. J. Lee, S. Sim, C. W. Lee, T. Choi, H. Jung, Y. Kim, Z. Lee, J.-M. Myoung, C. Dussarrat, C. Lansalot-Matras, J. Park, H. Choi, and H. Kim, Nat. Commun. 6, 7817 (2015).

[9] S. Manzeli, D. Ovchinnikov, D. Pasquier, O. V. Yazyev, and A. Kis, Nat. Rev. Mater. 2, 17033 (2017).

[10] C.-S. Lee, B. Cline, S. Sinha, G. Yeric, and H.-S. P. Wong, IEEE International Electron Devices Meeting (IEDM) 28.3.1-28.3.4 (2016).

[11] L. Yu, D. El-Damak, U. Radhakrishna, X. Ling, A. Zubair, Y. Lin, Y. Zhang, M.-H. Chuang, Y.-H. Lee, D. Antoniadis, J. Kong, A. Chandrakasan, and T. Palacios, Nano Lett. 16, 6349 (2016).

[12] S. Wachter, D. K. Polyushkin, O. Bethge, and T. Mueller, Nat. Commun. 8, 14948 (2017).

[13] K. F. Mak, and J. Shan, Nat. Photonics 10, 216 (2016).

[14] R. Kurapati, K. Kostarelos, M. Prato, and A. Bianco, Adv. Mater. 28, 6052 (2016).

[15] H. Guo, C. Lan, Z. Zhou, P. Sun, D. Wei, and C. Li, Nanoscale 9, 6246 (2017).

[16] O. V. Yazyev and A. Kis, Mater. Today 18, 20 (2015).

[17] F. Schwierz, J. Pezoldt, and R. Granzner, Nanoscale 7, 8261 (2015).

[18] A. K. Geim and I. V. Grigorieva, Nature 499, 419 (2013).

[19] M. Y. Li, C. H. Chen, Y. Shi, and L. J. Li, Mater. Today 19, 322 (2016).

[20] D. Chiappe , I. Asselberghs, S. Sutar, S. Iacovo, V. Afanas'ev, A. Stesmans, Y. Balaji, L. Peters, M. Heyne, M. Mannarino, W. Vandervorst, S. Sayan, C. Huyghebaert, M. Caymax, M. Heyns, S. De Gendt, I. Radu, and A. Thean, Adv. Mater. Interfaces 3, 1500635 (2016).

[21] D. Chiappe, J. Ludwig, A. Leonhardt, S. El Kazzi, A. N. Mehta, T. Nuytten, U. Celano, S. Sutar, G. Pourtois, M. Caymax, K. Paredis, W. Vandervorst, D. Lin, S. De Gendt, K. Barla, C. Huyghebaert, I. Asselberghs, and I. Radu, Nanotechnology 29, 425602 (2018).

[22] T. H. Ly, D. J. Perello, J. Zhao, Q. Deng, H. Kim, G. H. Han, S. H. Chae, H. Y. Jeong, and Y. H. Lee, Nat. Commun. 7, 10426 (2016).

[23] B. G. Shin, G. H. Han, S. J. Yun, H. M. Oh, J. J. Bae, Y. J. Song, C. Y. Park, and Y. H. Lee, Adv. Mater. 28 9378 (2016).

[24] M. Mongillo, D. Chiappe, G. Arutchelvan, I. Asselberghs, M. Perucchini, M. Manfrini, D. Lin, C. Huyghebaert, and I. Radu, Appl. Phys. Lett. 109, 233102 (2016).

[25] A. Stesmans, S. Iacovo, D. Chiappe, I. Radu, C. Huyghebaert, S. De Gendt, and V. V. Afanas'ev, Nanoscale Res. Lett. 12, 283 (2017).

[26] J. Hong, Z. Hu, M. Probert, K. Li, D. Lu, X. Yang, L. Gu, N. Mao, Q. Feng, L. Xie, J. Zhang, D. Wu, Z. Zhan, C. Jin, W. Ji, X. Zhang, J. Yuan, and Z. Zhang, Nat. Commun. 6, 6293 (2015).

[27] H.-P. Komsa and A. V. Krasheninnikov, Phys. Rev. B 91, 125304 (2015).

[28] D. Liu, Y. Guo, L. Fang, and J. Robertson, Appl. Phys. Lett. 103, 183113 (2013).

[29] X. Zou, Y. Liu, and B. Yakobson, Nano. Lett. 13, 253 (2013).

[30] W. Zhou, X. Zou, S. Najmaei, Z. Liu, Y. Shi, J. Kong, J. Lou, P. M. Ajayan, B. I. Yakobson, and J.-C. Idrobo, Nano Lett. 13, 2615 (2013).

[31] K. C. Santosh, R. C. Longo, R. Addou, R. M. Wallace, and R. M. Cho, Nanotechnol. 25, 375703 (2014).

[32] S. Haldar, H. Vovusha, M. K. Yadav, O. Eriksson, and B. Sanyal, Phys. Rev. B 92, 235408 (2015).

[33] S. C. Lu and J. P. Leburton, Nanoscale Res. Lett. 9, 676 (2014).

[34] R. Addou, L. Colombo, and R. M. Wallace, ACS Appl. Mater. Interfaces 7, 11921 (2015).

[35] X. Wei, Z. Yu, F. Hu, Y. Cheng, L. Yu, X. Wang, M. Xiao, J. Wang, X. Wang, and Y. Shi, AIP Adv. 4, 123004 (2014).

[36] S. McDonnell, R. Addou, C. Buie, R. M. Wallace, and C. L. Hinkle, ACS Nano 8, 2880 (2014).

[37] J. Sun, X. Li, W. Guo, M. Zhao, X. Fan, Y. Dong, C. Xu, J. Deng, and Y. Fu, Crystals 7, 198 (2017).

[38] A. Stesmans, S. Iacovo, and V. V. Afanas'ev, Appl. Phys. Lett. 109, 172104 (2016).

[39] B. Schoenaers, A. Stesmans, and V. V. Afanas'ev, AIP Advances 7, 105006 (2017).

[40] B. Schoenaers, A. Stesmans, and V. V. Afanas'ev, Phys. Status Solidi C 1700211 (2017).

[41] S. Iacovo, A. Stesmans, M. Houssa and V. V. Afanas'ev, J. Phys.: Condens. Matter 29, 08LT01 (2017).

[42] B. Schoenaers, A. Stesmans, and V. V. Afanas'ev, J. Vac. Sci. Technol. A 36, 05G503 (2018).

[43] M. Houssa, K. Iordanidou, G. Pourtois, V. V. Afanas'ev, and A. Stesmans, Appl. Surf. Sci. 416, 853 (2017).

[44] A. Stesmans, J. Magn. Reson. 76, 14 (1988).

[45] A. Stesmans, and V. V. Afanas'ev, J. Appl. Phys. 83, 2449 (1998).

[46] J. Wu, P. Cao, Z. Zhang, F. Ning, S. Zheng, J. He, and Z. Zhang, Nano Lett. 18, 1543 (2018).

[47] A. M. van der Zande, P. Y. Huang, D. A. Chenet, T. C. Berkelbach, Y. You,G. Lee, T. F. Heinz, D. R. Reichman, D. A. Muller, and J. C. Hone, Nat. Mater. 12, 554 (2013).

[48] D. Lv, H. Wang, D. Zhu, J. Lin, G. Yin, F. Lin, Z. Zhang, and C. Jin, Sci. Bull. 62, 846 (2017).

[49] W. L. Spychalski, M. Pisarek, and R. Szoszkiewicz, J. Phys. Chem. C 121, 26027 (2017).

[50] G. D. Clayton and F. E. Clayton in *Patty's Industrial Hygiene and Toxicology: Volume 2A, 2B, 2C: Toxicology* (3rd ed., John Wiley and Sons, New York, 1981), p. 1811.

[51] T. H. Ly, M. H. Chiu, M. Y. Li, J. Zhao, D. J. Perello, M. O. Cichocka, H. M. Oh, S. H. Chae, H. Y. Jeong, F. Yao, L. J. Liand, and Y. H. Lee, ACS Nano 8, 11401 (2014).

[52] D. Zhu, H. Shu, F. Jiang, D. Lv, V. Asokan, O. Omar, J. Yuan, Z. Zhang, and C. Jin, NPJ 2D Mater. Appl. 1, 8 (2017).